fluids

MDPI

Article

Numerical Evaluation of the IMERSPEC Methodology and Spalart–Allmaras Turbulence Model in Fully Developed Channel Flow Simulations

Laura Augusta Vasconcelos de Albuquerque [1,*,†], Mariana Fernandes dos Santos Villela [1,†] and Felipe Pamplona Mariano [2,†]

[1] Computational Engineering Group, Agreste Academic Center (CAA), Federal University of Pernambuco (UFPE), Avenida Marielle Franco, KM 59, s/n, Nova Caruaru, Caruaru 55014-900, PE, Brazil; mariana.villela@ufpe.br

[2] Laboratory of Thermal and Fluid Engineering (LATEF), School of Electrical, Mechanical and Computing Engineering (EMC), Federal University of Goiás (UFG), Avenida Esperança, Al. Ingá, Prédio B5, Campus Samambaia, Goiânia 74690-900, GO, Brazil; fpmariano@ufg.br

* Correspondence: laura.vasconcelos@ufpe.br

† These authors contributed equally to this work.

Abstract: This study evaluates the performance of the IMERSPEC methodology combined with the Spalart–Allmaras turbulence model for simulating fully developed turbulent flows in a plane channel. Turbulent flows, known for their complexity, require numerical methods that balance computational efficiency with accuracy. The IMERSPEC approach, recognized for its spectral accuracy and efficiency, was applied alongside the Spalart–Allmaras model, valued for its simplicity and robustness in representing turbulence, particularly in scenarios where flow over solid surfaces is critical. Simulations were conducted at Reynolds numbers (Re_τ) of 180, 550, and 1000, with results validated against direct numerical simulation (DNS) data. The study investigated various grid resolutions, revealing that finer meshes substantially enhance accuracy by mitigating velocity profile oscillations and reducing the L_2 error norm. Key findings highlight the method's ability to accurately replicate turbulent flow characteristics, including velocity distributions and shear stress profiles, while maintaining a favorable computational cost-to-accuracy ratio. This work provides valuable insights into turbulence modeling, demonstrating the potential of the IMERSPEC methodology for practical engineering applications.

Keywords: IMERSPEC methodology; Spalart–Allmaras turbulence model; turbulent-flow simulations

check for updates

Academic Editor: Giuliano De Stefano

Received: 16 December 2024
Revised: 24 January 2025
Accepted: 28 January 2025
Published: 11 February 2025

Citation: Albuquerque, L.A.V.d.; Villela, M.F.d.S.; Mariano, F.P. Numerical Evaluation of the IMERSPEC Methodology and Spalart–Allmaras Turbulence Model in Fully Developed Channel Flow Simulations. *Fluids* **2025**, *10*, 45. https://doi.org/10.3390/fluids10020045

Copyright: © 2025 by the authors. Licensee MDPI, Basel, Switzerland. This article is an open access article distributed under the terms and conditions of the Creative Commons Attribution (CC BY) license (https://creativecommons.org/licenses/by/4.0/).

1. Introduction

Most flows encountered in nature and practical engineering applications exhibit turbulent characteristics, characterized by pressure and velocity fluctuations superimposed on the mean flow. For instance, the boundary layer in the Earth's atmosphere is generally turbulent, except under highly stable conditions, while sub-surface ocean currents also exhibit turbulence [1]. Similarly, turbulent behavior is observed in the boundary layers formed around aircraft wings, vehicles, and in the flow of natural gas and oil through pipelines [2]. Understanding turbulence and its underlying physical mechanisms necessitates a detailed analysis of the temporal and spatial variations of these fluctuations [3,4]. Factors such as fluid viscosity and geometry play crucial roles in shaping the diverse turbulent structures observed in these flows [5].

Turbulence is a regime of dynamic systems characterized by a vast number of degrees of freedom. The inherent complexity of turbulent flows makes deterministic prediction challenging, thereby making statistical analysis the primary approach [5]. Turbulence typically occurs at high Reynolds numbers, with the transition to and maintenance of the turbulent regime depending on the interplay between convective and diffusive effects. Convective effects, which are highly nonlinear, amplify disturbances and generate instabilities, while diffusive effects, associated with viscous dissipation, stabilize the flow by inhibiting these instabilities [6]. The Reynolds number (Re) quantifies the relative importance of these competing effects: the inertial convective effects and the viscous diffusive effects. A flow transitions to or remains turbulent only when the Reynolds number surpasses a critical threshold. Additionally, turbulent flows are marked by high diffusivity, three-dimensional vorticity fluctuations, significant energy dissipation, continuity, and unpredictability [7].

The most commonly employed methodologies for analyzing turbulent flows are direct numerical simulation (DNS), large eddy simulation (LES), and Reynolds-averaged Navier–Stokes (RANS) modeling. These approaches follow a trade-off: as the cost of simulations decreases, the level of modeling complexity increases [8]. DNS resolves all flow scales directly but is constrained to low or moderate Reynolds numbers due to its high computational cost, making it particularly valuable for studying turbulent phenomena and developing more accurate models. In contrast, LES applies spatial filtering to the governing equations, enabling simulations in complex geometries and at higher Reynolds numbers, albeit with a substantially higher computational cost than RANS. The RANS approach, focusing on the effects of turbulence on mean flow properties, introduces time-averaging, resulting in Reynolds stresses that represent instantaneous fluctuations. This requires the development of closure models to account for these stresses and other turbulent scalar transport terms [8].

For engineering applications, the time-averaged properties of the flow, such as velocities, pressures, and mean stresses, are typically sufficient, eliminating the need to resolve detailed turbulent fluctuations. In this context, as noted by [9], most turbulent-flow simulations rely on methods based on the Reynolds-averaged Navier–Stokes (RANS) equations. The majority of RANS turbulence models are built upon the Boussinesq hypothesis, which relates the Reynolds stress tensor to the mean rate of strain tensor through an analogy with the constitutive equation of a Newtonian fluid [6]. In this analogy, the Reynolds stress tensor is proportional to the mean rate of strain tensor, with turbulent viscosity μ_t acting as the proportionality constant.

Turbulent viscosity μ_t can be modeled at various levels of complexity, generally as proportional to a characteristic velocity V_c and a characteristic length scale ℓ_c. These quantities can be determined using algebraic Equations (zero-order differential equations), as in the Prandtl mixing length model [6]. Alternatively, one or more differential equations can be employed for more advanced models.

In single-equation turbulent viscosity models, a differential equation is solved for a specific turbulent quantity, which is then used to determine the characteristic length and velocity scales, both of which are critical for evaluating turbulent viscosity. This viscosity is proportional to the density ρ, the velocity fluctuation V_L, and the characteristic turbulence length scale L, leading to the relationship $L_v \sim \rho V_L$. A well-known example of this class is the Spalart–Allmaras (SA) closure model, primarily developed for computational fluid dynamics (CFD) applications in aerospace, where flow over solid surfaces is of particular importance [5]. The SA model requires solving a differential equation for a modified turbulent viscosity coefficient, denoted as $\tilde{v}$. The SA model has shown reliable results in scenarios involving adverse pressure gradients and has gained popularity in wind turbine studies [10,11]. In comparison, while DNS models offer the highest accuracy,

they come with a high computational cost, particularly for higher Reynolds numbers. LES offers a middle ground in terms of computational cost and accuracy, suitable for complex geometries, whereas the SA model, being part of RANS-based methods, provides a computationally efficient alternative for scenarios where only mean flow properties are required.

To understand turbulent phenomena, computational fluid dynamics (CFD) relies on advanced techniques that use high-order accuracy methods, enabling the generation of results that closely represent the physical processes involved. Among these methods, spectral techniques are particularly notable for their ability to combine high accuracy with reduced computational costs compared to classical high-order methods, such as high-order finite difference and compact schemes [12]. This efficiency gain is made possible through the use of fast Fourier transform (FFT) [13]: while finite difference methods incur a computational cost of $O(N^2)$, where N is the number of grid points, FFT operates at a cost of $O(N \log_2 N)$ [12]. Moreover, the projection method [14,15] enables the calculation of the pressure field in spectral space, eliminating the need to solve the Poisson equation, one of the most computationally expensive steps in conventional simulations.

To address complex geometries and non-periodic boundary conditions, the immersed boundary method (IBM) [16] offers a highly effective solution. This approach introduces a source term that acts as a body force in the Navier–Stokes equations, allowing the representation of an immersed geometry within the flow without the need to modify the mesh [15]. The integration of the IBM and pseudospectral Fourier methods leads to the IMERSPEC approach [14,15]. In the physical domain, boundary conditions are applied using the IBM, while periodic boundary conditions, which are essential for FFT calculations, are enforced in the complementary external domain.

This study builds upon and extends the IMERSPEC methodology to simulate turbulent flows using the RANS equations coupled with the Spalart–Allmaras turbulence model. The simulations are validated by comparing the results with direct numerical simulation (DNS) data for plane channel flows at various Reynolds numbers. In doing so, this work enhances the understanding and application of IMERSPEC in capturing the complexities of turbulent flow behavior. The research contributes to the development of efficient and accurate computational fluid dynamics (CFD) methods, with potential applications in aerodynamic design, fluid dynamics research, and engineering analysis.

2. Mathematical Modeling and Numerical Method

Turbulent isothermal flows of Newtonian fluids are governed by the continuity and Navier–Stokes equations. For incompressible flows, these equations, subjected to a temporal averaging operator, are expressed in indicial notation as Equations (1) and (2):

$$\frac{\partial \bar{u}_i}{\partial x_i} = 0, \tag{1}$$

$$\frac{\partial \bar{u}_i}{\partial t} + \frac{\partial}{\partial x_j}(\bar{u}_i \bar{u}_j) = -\frac{1}{\rho}\frac{\partial \bar{p}}{\partial x_i} + \frac{\partial}{\partial x_j}\left[\nu\left(\frac{\partial \bar{u}_i}{\partial x_j} + \frac{\partial \bar{u}_j}{\partial x_i}\right) - \overline{u_i' u_j'}\right] + \frac{\bar{f}_i}{\rho}, \tag{2}$$

where $\bar{p}$ is the mean pressure [N/m^2], $\bar{u}_i$ is the mean velocity in the i-direction [m/s], $\bar{f}_i$ is a source term [N/m^3], ρ is the density [kg/m^3], ν is the kinematic viscosity [m^2/s], x_i represents the spatial coordinate (x or y) [m], and t is time [s].

The term $\overline{u_i' u_j'}$ in Equation (2), known as the Reynolds stress tensor, introduces closure issues due to its unknown nature. To address this, Boussinesq proposed a hypothesis that models the Reynolds stress tensor by drawing an analogy to the Stokes model for molecular viscous stresses [5]. The resulting model is given by Equation (3):

$$-\overline{u_i' u_j'} = \nu_t \left(\frac{\partial \bar{u}_i}{\partial x_j} + \frac{\partial \bar{u}_j}{\partial x_i} \right) + \frac{2}{3} k \delta_{ij}, \tag{3}$$

where $k = \frac{1}{2}\overline{u_i' u_i'}$ represents the turbulent kinetic energy, δ_{ij} is the Kronecker delta, and ν_t is the turbulent kinematic viscosity. Unlike molecular viscosity, an inherent fluid property, turbulent viscosity is a flow-dependent characteristic.

The turbulent viscosity ν_t can be determined using turbulence models such as Spalart–Allmaras, employed in this study. Additionally, the turbulent kinetic energy contributes to a modified pressure term, p^*, which combines the mean pressure and the turbulence effects. Considering these modifications, Equation (2) can be rewritten as:

$$\frac{\partial \bar{u}_i}{\partial t} + \frac{\partial}{\partial x_j}\left(\bar{u}_i \bar{u}_j\right) = -\frac{1}{\rho}\frac{\partial \bar{p}^*}{\partial x_i} + \frac{\partial}{\partial x_j}\left[(\nu + \nu_t) \left(\frac{\partial \bar{u}_i}{\partial x_j} + \frac{\partial \bar{u}_j}{\partial x_i} \right) \right] + \frac{\bar{f}_i}{\rho}. \tag{4}$$

2.1. Immersed Boundary Method—IBM

The immersed boundary method (IBM) employs two computational domains: the Eulerian and Lagrangian domains. In the Eulerian domain, the governing equations for fluid flow are solved; meanwhile, in the Lagrangian domain, the force field is evaluated to represent the immersed interface within the flow [15]. The interaction between these domains is facilitated through a source term added to the Navier–Stokes equations, as shown in Equation (4). This source term is defined throughout the Eulerian domain but is distributed based on its representation in the Lagrangian domain, as expressed in Equation (5).

$$f_i(\vec{x}, t) = \begin{cases} F_i(\vec{X}, t) & \text{if } \vec{x} = \vec{X}, \\ 0 & \text{if } \vec{x} \neq \vec{X}. \end{cases} \tag{5}$$

Here, $\vec{x}$ denotes the position of a fluid particle, while $\vec{X}$ represents the position of a particle adjacent to the solid interface, as illustrated in Figure 1. The source term assumes non-zero values exclusively at points coinciding with the immersed geometry, enabling the Eulerian field to detect the presence of the solid interface [14].

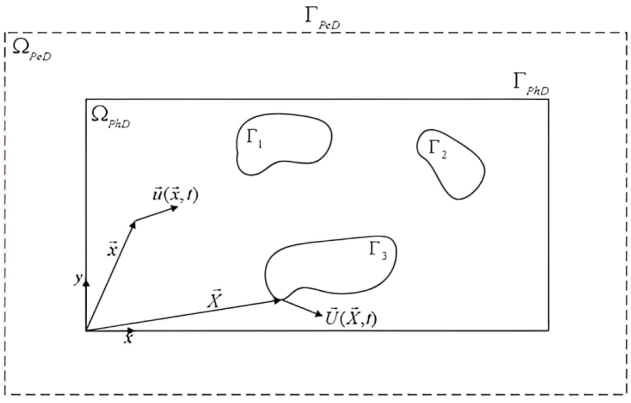


Figure 1. Schematic representation of the Eulerian and Lagrangian domains.

The multi-direct forcing (MDF) method, introduced by [17], is a refined approach to the immersed boundary framework employed in this study. This method enhances the calculation of the interface force $F_i(\vec{X}, t)$ through iterative refinement, significantly improving the accuracy of the Lagrangian force representation [15]. MDF is specifically designed to enforce the desired physical and numerical boundary conditions at the immersed interface with high precision. The interface force is derived directly from the governing momentum

equations, applied to the fluid particles residing at the fluid–solid boundary, as expressed in Equation (6). The notations and variables used are consistent with Equation (4), but the calculations are restricted to the Lagrangian interface (Γ) shown in Figure 1.

$$F_i(\vec{X},t) = \frac{\partial \bar{U}_i}{\partial t}(\vec{X},t) + \frac{\partial}{\partial X_j}(\bar{U}_i\bar{U}_j)(\vec{X},t) + \frac{1}{\rho}\frac{\partial \bar{P}^*}{\partial X_i}(\vec{X},t) - \frac{\partial}{\partial X_j}\left[(\nu+\nu_t)\left(\frac{\partial \bar{U}_i}{\partial X_j} + \frac{\partial \bar{U}_j}{\partial X_i}\right)\right]. \tag{6}$$

By employing the temporal parameter U^* introduced by [17] and discretizing the time operator, Equation (7) is obtained. It is important to note that the explicit Euler method is utilized for the time derivative in this equation, primarily for illustrative and didactic purposes. Nevertheless, in the present study, a more accurate fourth-order Runge–Kutta method is applied for time discretization [18].

$$F_i(\vec{X},t) = \frac{U_i(\vec{X},t+\Delta t) - U_i^*(\vec{X},t) + U_i^*(\vec{X},t) - U_i(\vec{X},t)}{\Delta t} + RHS_i(\vec{X},t). \tag{7}$$

where Δt is the timestep, and

$$RHS_i(\vec{X},t) = \frac{\partial}{\partial X_j}(\bar{U}_i\bar{U}_j)(\vec{X},t) + \frac{1}{\rho}\frac{\partial \overline{P^*}}{\partial X_i}(\vec{X},t) - \frac{\partial}{\partial X_j}\left[(\nu+\nu_t)\left(\frac{\partial \bar{U}_i}{\partial X_j} + \frac{\partial \bar{U}_j}{\partial X_i}\right)\right]. \tag{8}$$

Equation (7) is decomposed into Equations (9) and (10):

$$\frac{U_i^*(\vec{X},t) - U_i(\vec{X},t)}{\Delta t} + RHS_i(\vec{X},t) = 0, \tag{9}$$

$$F_i(\vec{X},t) = \frac{U_i(\vec{X},t+\Delta t) - U_i^*(\vec{X},t)}{\Delta t}. \tag{10}$$

Here, $U_i(\vec{X},t+\Delta t) = U_{\mathrm{FI}}$ is the velocity at the immersed boundary, and $U_i^*(\vec{X},t)$ is expressed as:

$$U_i(\vec{X},t) = \begin{cases} u_i^*(\vec{X},t) & \text{if } \vec{x} = \vec{X}, \\ 0 & \text{if } \vec{x} \neq \vec{X}. \end{cases} \tag{11}$$

Equation (9) is solved in the Eulerian domain using the Fourier spectral space. The intermediate velocity $u_i^*(\vec{x},t)$ is interpolated onto the Lagrangian domain, resulting in $U_i^*(\vec{X},t)$ as per Equation (10). This value is subsequently mapped back to the Eulerian collocation points, and the final velocities in the Eulerian domain are updated using Equation (12).

$$u_i(\vec{x},t+\Delta t) = u_i^*(\vec{x},t) + \Delta t f_i. \tag{12}$$

2.2. Fourier Pseudospectral Method—FPSM

Equations (1) and (4) in Fourier space are expressed as Equations (13) and (14), respectively:

$$\frac{\widehat{\partial \bar{u}_j}}{\partial x_j} = ik_j\widehat{\bar{u}}_j = 0, \tag{13}$$

$$\widehat{\frac{\partial \bar{u}_i}{\partial t}} = -\widehat{\frac{\partial}{\partial x_j}(\bar{u}_i\bar{u}_j)} - \frac{1}{\rho}\widehat{\frac{\partial \bar{p}^*}{\partial x_i}} + \frac{\partial}{\partial x_j}\left[\nu_{ef}\left(\widehat{\frac{\partial \bar{u}_i}{\partial x_j}} + \frac{\partial \bar{u}_j}{\partial x_i}\right)\right] + \frac{\widehat{\bar{f}}_i}{\rho}. \tag{14}$$

where k_j and $\widehat{\bar{u}}_j$ denote the wave vector and the Fourier-transformed velocity vector, respectively, and $\nu_{ef} = \nu + \nu_t$.

Equation (13) establishes the orthogonality between the wave number vector, k_i, and the transformed velocity, $\widehat{\bar{u}_i}(\vec{k},t)$. This relationship defines a divergence-free vector plane, referred to as the π-plane, which is orthogonal to the wave number vector and contains the transformed velocity [5]. Analyzing the components of Equation (14) reveals distinct spatial orientations: the transient and viscous terms lie within the π-plane, while the pressure gradient term is perpendicular to it. The orientation of the nonlinear term, however, remains initially undetermined. By combining all components of Equation (14), the equation is resolved as follows:

$$\underbrace{\left(\frac{\partial \widehat{\bar{u}_i}}{\partial t}\right)}_{\in\pi} + \underbrace{\left(\frac{\partial \widehat{(\bar{u}_i\bar{u}_j)}}{\partial x_j} + ik_i\widehat{\bar{p}^*} - \frac{\partial}{\partial x_j}\left[\nu_{ef}\left(\widehat{\frac{\partial \bar{u}_i}{\partial x_j}} + \frac{\partial \bar{u}_j}{\partial x_i}\right)\right] + \frac{\widehat{\bar{f}_i}}{\rho}\right)}_{\in\pi} = 0. \tag{15}$$

Equation (15) implies:

$$\frac{\partial \widehat{(\bar{u}_i\bar{u}_j)}}{\partial x_j} + ik_i\widehat{\bar{p}^*} - \frac{\partial}{\partial x_j}\left[\nu_{ef}\left(\widehat{\frac{\partial \bar{u}_i}{\partial x_j}} + \frac{\partial \bar{u}_j}{\partial x_i}\right)\right] + \frac{\widehat{\bar{f}_i}}{\rho} = \wp_{im}\left[\frac{\partial \widehat{(\bar{u_m}\bar{u}_j)}}{\partial x_j} - \frac{\partial}{\partial x_j}\left[\nu_{ef}\left(\widehat{\frac{\partial \bar{u_m}}{\partial x_j}} + \frac{\partial \bar{u}_j}{\partial x_m}\right)\right] + \frac{\widehat{\bar{f}_i}}{\rho}\right], \tag{16}$$

where $\wp_{im}$ is the projection tensor. The pressure gradient term lies orthogonal to the π-plane, decoupling the pressure and velocity fields in Fourier space. Nevertheless, the pressure field can be reconstructed via post-processing, as detailed by [15].

The nonlinear term introduces a product of transformed functions which, based on the properties of Fourier transforms, corresponds to a convolution operation. This operation is represented as a convolution integral, whose computational solution is expensive compared to other methods. To reduce this cost, the pseudospectral Fourier method is utilized. In this approach, the momentum equation in Fourier space, formulated using the projection method, is expressed as:

$$\frac{\partial \widehat{\bar{u}_i}(\vec{k},t)}{\partial t} = -ik_j\wp_{im}\int_{\vec{k}=\vec{r}+\vec{s}} \widehat{\bar{u}_m}(\vec{r})\widehat{\bar{u}_j}(\vec{k}-\vec{r})\,d\vec{r} + ik_j\wp_{im}\int_{\vec{k}=\vec{r}+\vec{s}} \widehat{\nu_{ef}}(\vec{r})\left(\widehat{\frac{\partial \bar{u}_m}{\partial x_j}} + \frac{\partial \bar{u}_j}{\partial x_m}\right)(\vec{k}-\vec{r})\,d\vec{r}. \tag{17}$$

The nonlinear term can be treated in various forms. Among these, the skew–symmetric formulation is preferred due to its superior stability and accuracy [19]. In this study, the pseudospectral method is employed to solve the nonlinear term, wherein the velocity product is computed in physical space and subsequently transformed back into spectral space.

2.3. The Spalart–Allmaras Turbulence Model

The Spalart–Allmaras (SA) turbulence model was developed and calibrated using empirical data from a variety of flow configurations, guided by principles of dimensional analysis [5]. This model is formulated around a transport equation for the auxiliary variable $\tilde{\nu}$, as presented in Equation (18), with the transition terms excluded, as they are generally negligible in fully developed turbulent flows, which is consistent with the focus of the present study.

$$\frac{\partial \tilde{\nu}}{\partial t} + \frac{\partial}{\partial x_j}(u_j\tilde{\nu}) = C_{b1}\tilde{S}\tilde{\nu} - C_{w1}f_w\left(\frac{\tilde{\nu}}{d}\right)^2 + \frac{1}{\sigma}\left[\frac{\partial}{\partial x_j}\left((\nu+\tilde{\nu})\frac{\partial \tilde{\nu}}{\partial x_j}\right) + C_{b2}\frac{\partial \tilde{\nu}}{\partial x_j}\frac{\partial \tilde{\nu}}{\partial x_j}\right]. \tag{18}$$

The terms on the right-hand side of Equation (18) correspond, respectively, to the production, destruction, molecular and turbulent diffusion, and dissipation of viscosity. In this context, d denotes the distance to the nearest wall. The turbulent viscosity ν_t is

calculated using the modified viscosity $\tilde{\nu}$, incorporating a damping function f_{ν_1} to account for near-wall effects:

$$\nu_t = \tilde{\nu} f_{\nu_1}, \tag{19}$$

where

$$f_{\nu_1} = \frac{\chi^3}{\chi^3 + C_{\nu_1}^3}, \tag{20}$$

and

$$\chi = \frac{\tilde{\nu}}{\nu}. \tag{21}$$

Far from the wall, the damping function f_{ν_1} asymptotically approaches unity, reducing ν_t to $\tilde{\nu}$. The production term depends on the distance from the wall and is modulated by the function f_{ν_2}, which is defined as:

$$\tilde{S} = S + \frac{\tilde{\nu}}{\kappa^2 d^2} f_{\nu_2}, \tag{22}$$

where

$$f_{\nu_2} = 1 - \frac{\chi}{1 + \chi f_{\nu_1}}. \tag{23}$$

In Equation (22), the mean rate of strain S is defined in terms of the vorticity tensor Ω:

$$S = \sqrt{2\Omega_{ij}\Omega_{ij}}, \tag{24}$$

where

$$\Omega_{ij} = \frac{1}{2}\left(\frac{\partial u_i}{\partial x_j} - \frac{\partial u_j}{\partial x_i}\right). \tag{25}$$

The wall function f_w, which plays a crucial role near the boundary layer, amplifies the production term in proximity to the wall and diminishes in magnitude as the distance from the wall increases. It is defined as:

$$f_w = g\left[\left(1 + \frac{C_{w3}^6}{g^6 + C_{w3}^6}\right)^{\frac{1}{6}}\right], \tag{26}$$

where

$$g = r + C_{w2}(r^6 - r), \tag{27}$$

and

$$r = \frac{\tilde{\nu}}{\tilde{S}\kappa^2 d^2}. \tag{28}$$

The model relies on empirical constants, summarized in Table 1, which are calibrated based on well-known flows, especially turbulent boundary layers:

Table 1. Values of the constants used in the equations.

Constant	Value
C_{w1}	$\frac{C_{b1}}{\kappa^2} + \frac{1+C_{b2}}{\sigma}$
C_{w2}	0.3
C_{w3}	2
κ	0.41
C_{v1}	7.1
σ	$\frac{2}{3}$

Table 1. *Cont.*

Constant	Value
C_{b1}	0.1355
C_{b2}	0.622
C_{t1}	1
C_{t2}	2
C_{t3}	1.1
C_{t4}	2

In this study, the Spalart–Allmaras equation (Equation (18)) is solved using the Fourier pseudospectral method, necessitating a transformation of the equation into spectral space. Fourier transform is applied to the dependent variables, thereby converting the spatial derivatives into multiplications by complex numbers corresponding to the frequencies in spectral space.

The time derivative of $\tilde{\nu}$ in physical space is directly transformed as:

$$\frac{\partial \tilde{\nu}}{\partial t} \rightarrow \frac{\partial \hat{\tilde{\nu}}}{\partial t}. \tag{29}$$

The convective term is transformed by applying the derivative property of Fourier transform:

$$\frac{\partial(\overline{u_j}\tilde{\nu})}{\partial x_j} \rightarrow ik_j\widehat{\overline{u_j}\tilde{\nu}}. \tag{30}$$

The production and destruction terms are transformed into spectral space as follows:

$$c_{b1}\tilde{S}\tilde{\nu} \rightarrow c_{b1}\widehat{\tilde{S}\tilde{\nu}}, \tag{31}$$

$$-C_{w1}f_w\left(\frac{\tilde{\nu}}{d}\right)^2 \rightarrow -C_{w1}f_w\widehat{\left(\frac{\tilde{\nu}}{d}\right)^2}. \tag{32}$$

The viscous diffusion term is transformed into spectral space by considering the application of the derivative and convolution in spectral space:

$$\frac{1}{\sigma}\frac{\partial}{\partial x_j}\left[(\nu+\tilde{\nu})\frac{\partial \tilde{\nu}}{\partial x_j}\right] \rightarrow \frac{1}{\sigma}ik_j\left(\widehat{(\nu+\tilde{\nu})} * \left(ik_j\hat{\tilde{\nu}}\right)\right). \tag{33}$$

Finally, the turbulent diffusion term is transformed into Fourier spectral space as:

$$\frac{c_{b2}}{\sigma}\left(\frac{\partial \tilde{\nu}}{\partial x_j}\frac{\partial \tilde{\nu}}{\partial x_j}\right) \rightarrow \frac{c_{b2}}{\sigma}k_j^2\left(\hat{\tilde{\nu}}\right)^2. \tag{34}$$

Thus, the Spalart–Allmaras equation in spectral space can be written as:

$$\frac{\partial \hat{\tilde{\nu}}}{\partial t} + ik_j\widehat{\overline{u_j}\tilde{\nu}} = c_{b1}\widehat{\tilde{S}\tilde{\nu}} - C_{w1}f_w\widehat{\left(\frac{\tilde{\nu}}{d}\right)^2} - \frac{1}{\sigma}ik_j\left(\widehat{(\nu+\tilde{\nu})} * \left(ik_j\hat{\tilde{\nu}}\right)\right) + \frac{c_{b2}}{\sigma}k_j^2\left(\hat{\tilde{\nu}}\right)^2. \tag{35}$$

The pseudospectral method is employed to handle products of two functions. This process involves transforming the functions into physical space through the inverse Fourier transform, performing the product in physical space, and subsequently transforming the result back into spectral space.

Nonlinear terms are treated by the pseudospectral method in a skew–symmetric form, the most stable approach considered by [20]. The skew–symmetric form consists of calculating the arithmetic mean of the nonlinear term expressed both in the conservative and non-conservative forms. Specifically, we have:

- Divergent form: In the divergent form, the terms are written as derivatives of a flow. For the Spalart–Allmaras equation, the convective term in the conservative form is given by:
$$\frac{\partial(\bar{u_j}\tilde{\nu})}{\partial x_j} = ik_j\widehat{(\bar{u_j}\tilde{\nu})}, \tag{36}$$
- Non-divergent form: In the non-divergent form, the terms are expressed directly in terms of the derivative of the product of the functions:
$$\bar{u_j}\frac{\partial\tilde{\nu}}{\partial x_j} = \widehat{\bar{u_j}ik_j\tilde{\nu}}. \tag{37}$$

The skew–symmetric form combines the two previous approaches, resulting in an expression that minimizes numerical errors associated with spectral derivatives:

$$ik_j\widehat{\bar{u_j}\tilde{\nu}} = \frac{1}{2}\left[ik_j\widehat{(\bar{u_j}\tilde{\nu})} + \widehat{\bar{u_j}ik_j\tilde{\nu}}\right]. \tag{38}$$

This skew–symmetric treatment preserves the balance of the essential physical properties of the flow, while providing enhanced numerical stability.

The imposition of boundary conditions for the modified turbulent viscosity $\tilde{\nu}$ is achieved using the immersed boundary method, which treats the boundary conditions as additional force sources within the computational domain. This is accomplished by introducing a virtual force that acts on the variable $\tilde{\nu}$, guiding it to satisfy the imposed boundary condition. In the case of the no-slip condition, the force is applied in such a way that the tangential velocity at the wall is zero.

In the Spalart–Allmaras equation, the imposition of a no-slip boundary condition can be mathematically represented by modifying the convective term in the transport equation for $\tilde{\nu}$, as follows:

$$\frac{\partial\tilde{\nu}}{\partial t} + \frac{\partial(\bar{u_j}\tilde{\nu})}{\partial x_j} = c_{b1}\tilde{S}\tilde{\nu} - C_{w1}f_w\left(\frac{\tilde{\nu}}{d}\right)^2 + \frac{1}{\sigma}\frac{\partial}{\partial x_j}\left[(\nu+\tilde{\nu})\frac{\partial\tilde{\nu}}{\partial x_j}\right] + \frac{c_{b2}}{\sigma}\left(\frac{\partial\tilde{\nu}}{\partial x_j}\frac{\partial\tilde{\nu}}{\partial x_j}\right) + f_{bc}, \tag{39}$$

where $\mathbf{f}_{bc}$ represents the virtual force imposed to satisfy the no-slip condition. This force is calculated iteratively to ensure that $\tilde{\nu}$ reaches the desired value at the boundary:

$$f_{bc} = -\lambda(\tilde{\nu} - \tilde{\nu}_{bc}), \tag{40}$$

where λ is a control parameter that adjusts the intensity of the applied force, and $\tilde{\nu}_{bc}$ is the reference value of $\tilde{\nu}$ at the boundary, which is zero for the no-slip condition.

The MDF is used to iteratively adjust the virtual force in order to correct any deviation from the desired boundary condition. Each successive application of the force brings $\tilde{\nu}$ closer to the reference value at the boundary, thus ensuring the exact imposition of the no-slip condition.

3. Results

This study investigates fully developed, incompressible, statistically steady, and homogeneous turbulent flow in the axial direction (x). The predictions are validated against direct numerical simulation (DNS) data from [21,22], which provided a detailed examination of

this flow. The Reynolds numbers (Re_τ), defined based on the friction velocity (u_τ), were set at 180, 950, and 1000. According to [23], a value of $Re_\tau \sim 180$ is commonly estimated as the transition point between laminar and turbulent flow in channel configurations. Figure 2 depicts the geometry and coordinate system used in the analysis.

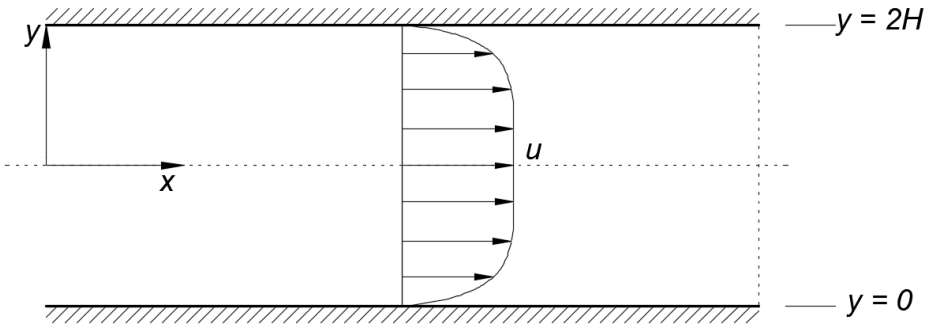


Figure 2. Geometry for turbulent flow in a plane channel.

The flow is modeled as incompressible, with no heat transfer, within a plane channel of axial length $L_x = 10$ m and width $L_y = 1$ m. It is treated as two-dimensional on average, neglecting edge effects in the direction normal to the study plane. This test case is particularly appropriate because the Spalart–Allmaras turbulence model was specifically calibrated to capture the characteristics of channel flows. Therefore, a robust implementation of the SA model using the IMERSPEC methodology is expected to produce results closely aligned with DNS data.

To assess the computational performance and predictive accuracy of the model in two-dimensional simulations, a uniform grid of 64×128 cells was employed. At the walls, a no-slip condition was imposed for the velocities u and vs., while periodic boundary conditions were applied in the axial direction (x). The solution was computed under a prescribed mean pressure gradient ($\Delta p = 0$) to achieve the desired Reynolds number. The initial condition for the simulation assumed a uniform flow across the entire domain.

The kinematic viscosity was defined as $\nu = \frac{1}{Re}$, and the inflow velocity U_∞ was set to 1.0 m/s. Initially, the stream-wise velocity component u was uniformly set to the inflow velocity throughout the domain, while the vertical velocity component vs. was initialized to zero. At the upper and lower walls, the no-slip condition ensured that $u = 0$. This condition was enforced using the immersed boundary method at each time step. To maintain a Courant–Friedrichs–Lewy (CFL) number of approximately 0.1 across the domain, a time step of $\Delta t = 2 \times 10^{-4}$ s was chosen, corresponding to a dimensionless time step $\Delta t^* = 2.8 \times 10^{-2}$; this was based on the mean velocity and half the channel height (H).

From the initial velocity field, the governing equations were integrated in time until the numerical solution reached a statistically steady state. The attainment of this state was determined by monitoring the convergence behavior of key parameters, such as the wall shear stress and the mean velocity at the channel center line ($y = H$). Statistical steady-state conditions were confirmed when these parameters displayed negligible variations over time, exhibiting approximately periodic behavior.

Figure 3 presents the normalized mean velocity profile as a function of the normalized distance across the channel width for fully developed flow at $Re_\tau = 1000$, compared to DNS data. Similarly, Figure 4 shows the viscous shear stress profile for $Re_\tau = 1000$, also compared with DNS data. For $Re_\tau = 550$, the corresponding mean velocity and shear stress profiles are displayed in Figures 5 and 6, respectively. For $Re_\tau = 180$, the mean velocity profile is shown in Figure 7, while Figure 8 presents the viscous shear stress profile.

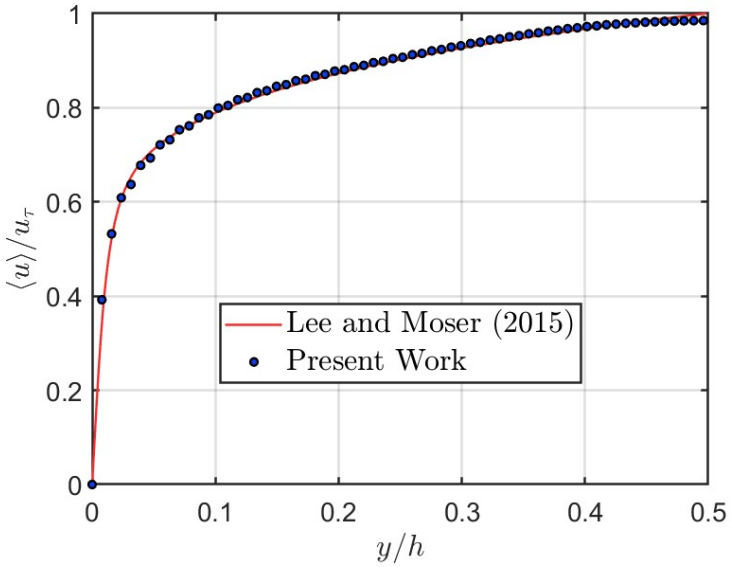


Figure 3. Normalized mean velocity profile for $Re_\tau = 1000$, compared with the results of [21].

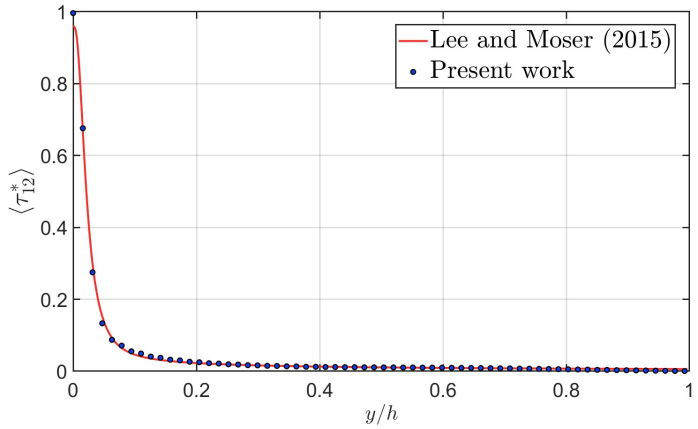


Figure 4. Viscous shear stress profile for $Re_\tau = 1000$, compared with the results of [21].

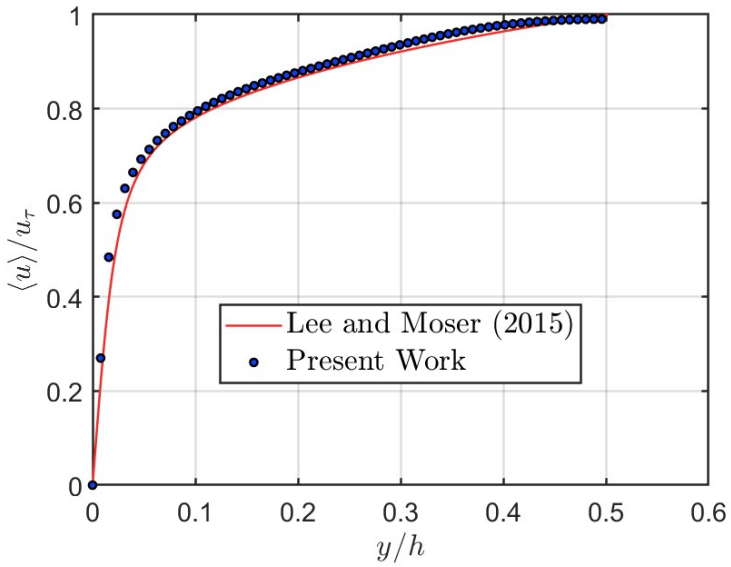


Figure 5. Normalized mean velocity profile for $Re_\tau = 550$, compared with the results of [21].

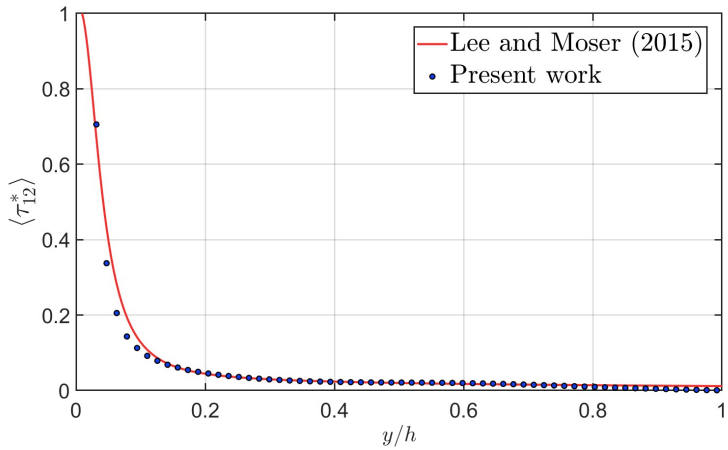


Figure 6. Viscous shear stress profile for $Re_\tau = 550$, compared with the results of [21].

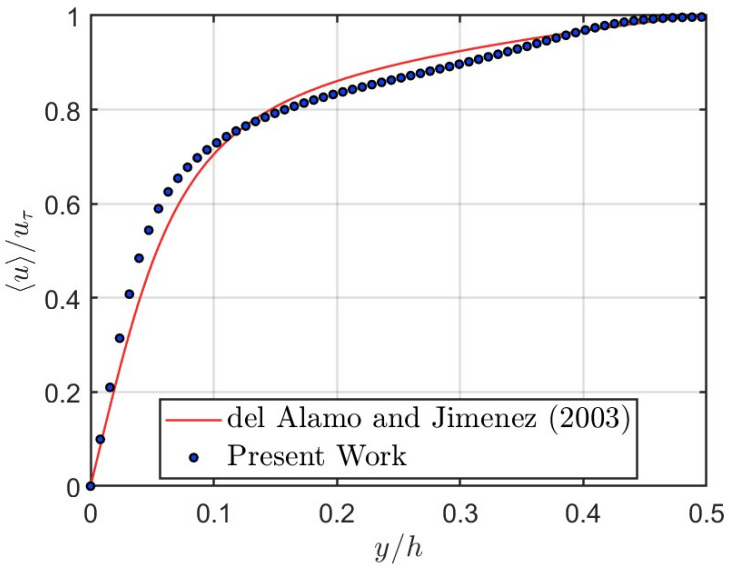


Figure 7. Normalized mean velocity profile for $Re_\tau = 180$, compared with the results of [22].

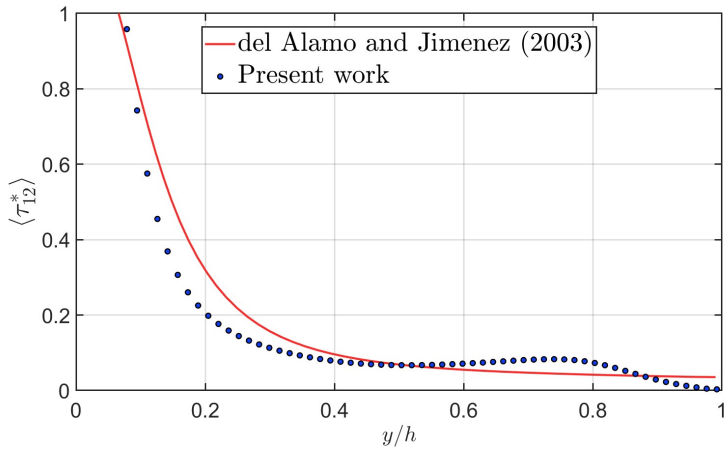


Figure 8. Viscous shear stress profile for $Re_\tau = 180$, compared with the results of [22].

As the flow reaches a fully turbulent state, the agreement with DNS data improves. With an increase in the Reynolds number, the flow becomes progressively more turbulent, leading to higher turbulent stresses. Additionally, the mean velocity profile becomes more uniform across the channel height due to enhanced momentum transfer in the y-direction.

For $Re_\tau = 1000$, simulations were conducted using different mesh configurations to evaluate the impact of spatial resolution on the accuracy of the results. Figures 9–12 show the mean velocity profiles obtained for meshes with resolutions of 64×32, 64×64, 64×128, and 64×256 grid points.

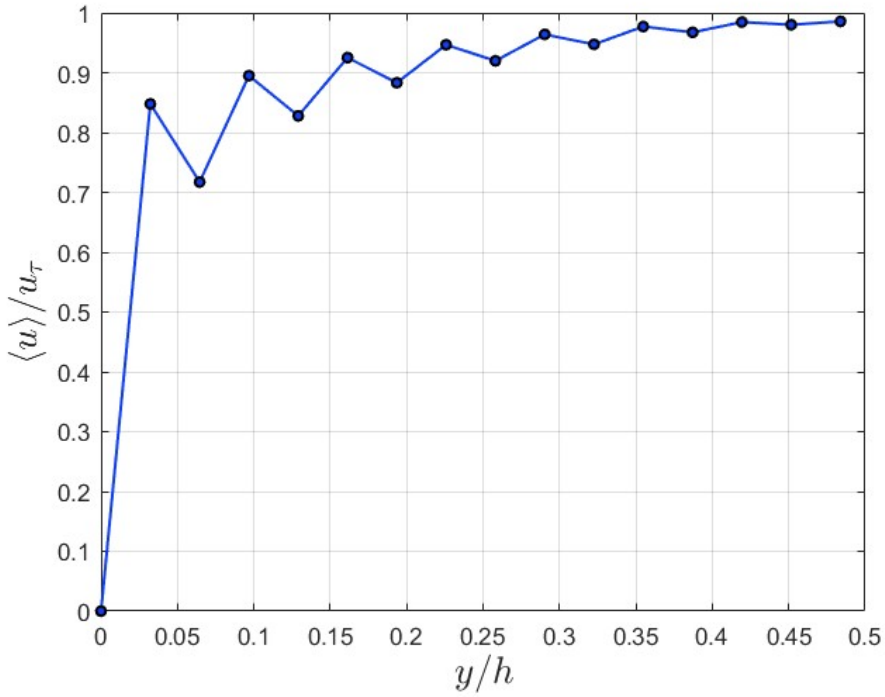


Figure 9. Mean velocity profile for $Re_\tau = 1000$ with a 64×32 mesh.

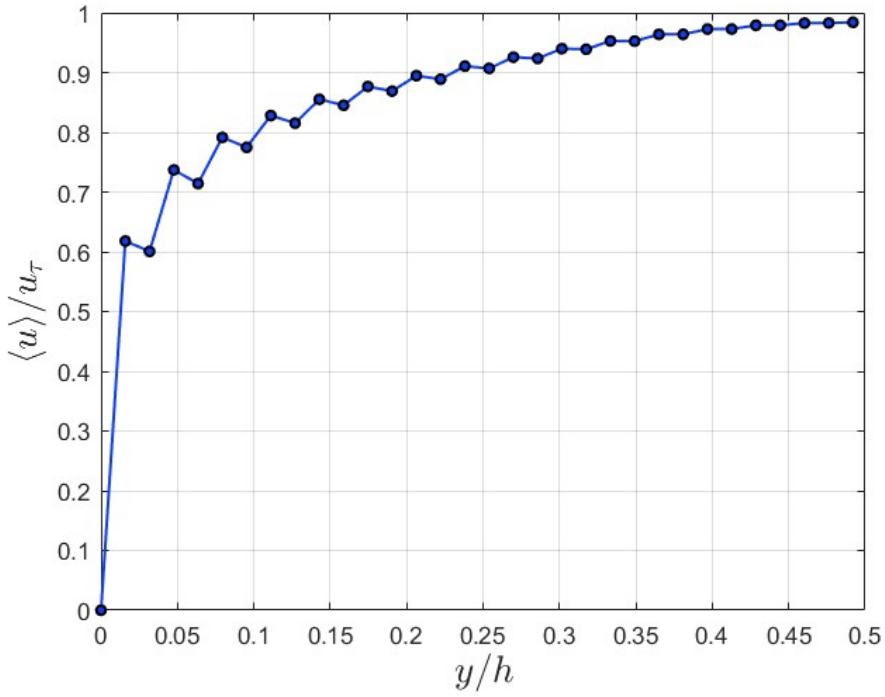


Figure 10. Mean velocity profile for $Re_\tau = 1000$ with a 64×64 mesh.

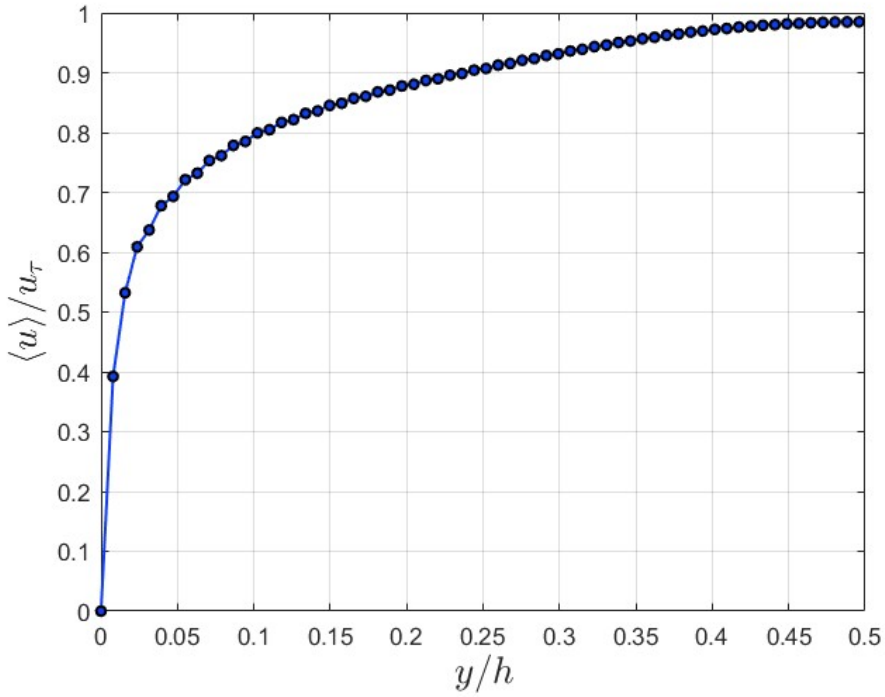


Figure 11. Mean velocity profile for $Re_\tau = 1000$ with a 64×128 mesh.

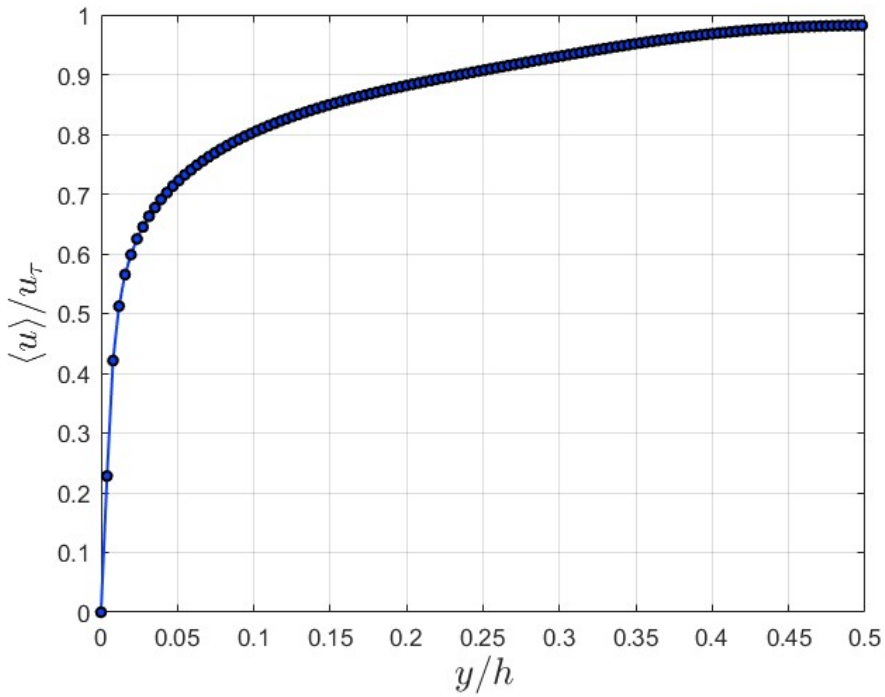


Figure 12. Mean velocity profile for $Re_\tau = 1000$ with a 64×256 mesh.

The results presented in Figures 9–11 reveal the presence of oscillations in the velocity profiles, particularly in coarser meshes such as 64×32 and 64×64. These oscillations are characteristic of spectral methods, which tend to be highly sensitive to mesh resolution, especially in high-Reynolds-number turbulent-flow simulations. This observation underscores the necessity for finer meshes to better capture the dynamic behavior associated with turbulence.

For the 64×128 mesh, the L_2 norm, which quantifies the difference between the numerical results and the reference DNS data, was found to be 1.992×10^{-2}. Using the

finer 64×256 mesh, this error was significantly reduced to $L_2 = 5.176 \times 10^{-3}$, highlighting the substantial improvement in accuracy with increased mesh resolution. These results emphasize the crucial role of mesh refinement in obtaining numerical solutions that better approximate the physical reality represented by DNS data. For reference, the mesh used in the DNS simulation was $n_x = 10{,}240$ and $n_z = 7680$ [21].

Figure 13 illustrates the velocity field for $Re_\tau = 1000$, showcasing the typical behavior of a fully developed turbulent flow. In this flow regime, the transverse velocity gradient reflects the intense momentum transfer in the direction normal to the main flow, resulting in a flatter velocity profile across the channel cross-section. This behavior aligns with the expected dynamics for high-Reynolds-number flows in channels, where turbulent stresses play a dominant role in the redistribution of momentum.

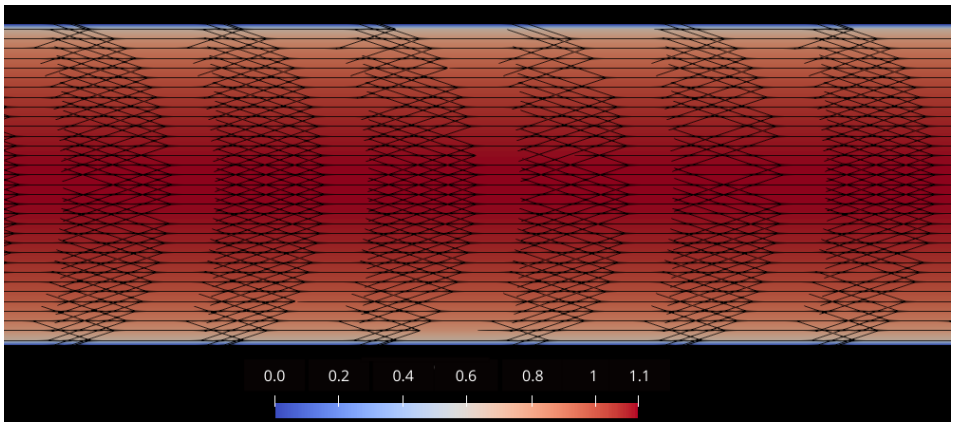


Figure 13. Velocity field for $Re_\tau = 1000$.

4. Discussion

The results underscore the effectiveness of the Spalart–Allmaras turbulence model, implemented using the IMERSPEC methodology, in accurately capturing the key characteristics of turbulent flow in plane channels. Validation against direct numerical simulation (DNS) data from the literature [21,22] demonstrated strong agreement, particularly for simulations conducted with refined mesh configurations.

Mesh refinement tests at $Re_\tau = 1000$ highlighted the sensitivity of the spectral method to spatial resolution. For coarser meshes (64×32 and 64×64), oscillations appeared in the mean velocity profiles, indicating that, while the spectral method provides high accuracy and convergence efficiency, achieving reliable results requires sufficient spatial refinement to resolve the intricate dynamics of turbulent flows. Conversely, finer meshes (64×128 and 64×256) yielded significantly improved agreement with DNS data, as evidenced by a marked reduction in the L_2 norm error. This improvement demonstrates the importance of mesh refinement in accurately capturing momentum exchange and velocity gradients characteristic of turbulent regimes.

The mean velocity profiles and viscous shear stresses confirmed the expected behavior of fully developed turbulent flows. At higher Reynolds numbers, turbulence intensity increases, resulting in greater momentum redistribution in the transverse direction and flatter velocity profiles. These findings align with previous DNS studies, which emphasize the predominance of turbulent stresses in the dynamics of high-Reynolds-number flows. The results further reinforce the suitability of the Spalart–Allmaras model in scenarios where flow over solid boundaries and high Reynolds numbers are critical, making it a robust choice for practical engineering applications.

5. Conclusions

This study demonstrated that the IMERSPEC methodology, combined with the Spalart–Allmaras turbulence model, is a highly promising approach for simulating turbulent flows in simplified geometries, particularly for applications that demand a balance between computational efficiency and accuracy. The results highlight the method's ability to accurately capture the key characteristics of turbulent flows while maintaining manageable computational costs.

Future research should focus on extending this methodology to more complex and realistic geometries, such as flows around cylinders and airfoils. Additionally, the development and implementation of advanced mesh refinement strategies could enhance the computational efficiency of the spectral method without sacrificing accuracy. Investigating the integration of other turbulence models with the IMERSPEC methodology also holds significant potential, as it would enable the exploration of a broader range of turbulent scales and flow regimes. Moreover, extending the approach to three-dimensional simulations represents a critical next step for achieving a more comprehensive understanding and modeling of turbulent phenomena.

The findings of this work not only affirm the effectiveness of combining the Spalart–Allmaras model with the IMERSPEC methodology but also lay a strong foundation for future studies involving more complex flow scenarios. This contributes meaningfully to the ongoing advancement of computational fluid dynamics, particularly in the simulation of turbulent flows.

Author Contributions: Conceptualization, L.A.V.d.A., F.P.M. and M.F.d.S.V.; Methodology, F.P.M., M.F.d.S.V. and L.A.V.d.A.; Software, F.P.M. and L.A.V.d.A.; Validation, L.A.V.d.A.; Formal analysis, L.A.V.d.A.; Investigation, L.A.V.d.A.; Resources, F.P.M.; Data curation, L.A.V.d.A.; Writing—original draft, L.A.V.d.A.; Writing—review and editing, M.F.d.S.V.; Supervision, M.F.d.S.V.; Project administration, M.F.d.S.V.; Funding acquisition, F.P.M. All authors have read and agreed to the published version of the manuscript.

Funding: This research was funded by Eletrobras and the Research and Technological Development Program (P&D) of ANEEL, under grant number ANEEL PD-00394-1906/2019.

Institutional Review Board Statement: Not applicable.

Informed Consent Statement: Not applicable.

Data Availability Statement: Data can be accessed upon request to any author of this manuscript.

Acknowledgments: The authors gratefully acknowledge the support of Eletrobras and the ANEEL Research and Technological Development Program (P&D) in the development of this work.

Conflicts of Interest: The authors declare no conflicts of interest.

References

1. Ruan, X. Note on the Bulk Estimate of the Energy Dissipation Rate in the Oceanic Bottom Boundary Layer. *Fluids* **2022**, *7*, 82. [CrossRef]
2. Tennekes, H.; Lumley, J.L. *A First Course in Turbulence*; The MIT Press: Cambridge, MA, USA, 1972.
3. Abramov, R.V. Turbulence via Intermolecular Potential: Viscosity and Transition Range of the Reynolds Number. *Fluids* **2023**, *8*, 101. [CrossRef]
4. Sofiadis, G.; Sarris, I. Turbulence Intensity Modulation by Micropolar Fluids. *Fluids* **2021**, *6*, 195. [CrossRef]
5. Silveira Neto, A. *Escoamentos Turbulentos—Análise Física e Modelagem Teórica*; Composer: Uberlândia, Brazil, 2020.
6. Pope, S.B. *Turbulent Flows*; Cambridge University Press: Cambridge, UK, 2000.
7. Kadivar, M.; Tormey, D.; McGranaghan, G. A review on turbulent flow over rough surfaces: Fundamentals and theories. *Int. J. Thermofluids* **2021**, *10*, 100077. [CrossRef]

8. Magalhães, G.M. Modelagem Matemática e Computacional de Escoamentos Turbulentos Multifásicos em Malha Adaptativa Bloco Estruturada Utilizando Método Multi Direct Forcing. Master's Thesis, Universidade Federal de Uberlândia, Uberlândia, Brazil, 2022.
9. Versteeg, H.K.; Malalasekera, W. *An Introduction to Computational Fluid Dynamics: The Finite Volume Method*; Pearson Education: Harlow, UK, 2007.
10. D'Alessandro, V.; Montelpare, S.; Ricci, R.; Zoppi, A. Numerical modeling of the flow over wind turbine airfoils by means of Spalart–Allmaras local correlation based transition model. *Energy* **2017**, *130*, 402–419. [CrossRef]
11. D'Alessandro, V.; Montelpare, S.; Ricci, R. Assessment of a Spalart–Allmaras Model Coupled with Local Correlation Based Transition Approaches for Wind Turbine Airfoils. *Appl. Sci.* **2021**, *11*, 1872. [CrossRef]
12. Canuto, C.; Hussaini, M.Y.; Quarteroni, A.; Zang, T.A. *Spectral Methods: Evolution to Complex Geometries and Applications to Fluid Dynamics*, 1st ed.; Springer: Berlin, Germany, 2007.
13. Cooley, J.W.; Tukey, J.W. An algorithm for the machine calculation of complex Fourier series. *Math. Comput.* **1965**, *19*, 297–301. [CrossRef]
14. Nascimento, A.A.; Mariano, F.P.; Padilla, E.L.M.; Silveira-Neto, A. Comparison of the convergence rates between Fourier pseudospectral and finite volume method using Taylor-Green vortex problem. *J. Braz. Soc. Mech. Sci. Eng.* **2020**, *42*, 491. [CrossRef]
15. Mariano, F.P.; de Queiroz Moreira, L.; Nascimento, A.A.; Silveira-Neto, A. An improved immersed boundary method by coupling of the multi-direct forcing and Fourier pseudospectral methods. *J. Braz. Soc. Mech. Sci. Eng.* **2022**, *44*, 388. [CrossRef]
16. Peskin, C.S. Flow patterns around heart valves: A numerical method. *J. Comput. Phys.* **1972**, *10*, 252–271. [CrossRef]
17. Wang, J.; Fan, J.; Luo, K. Combined multi-direct forcing and immersed boundary method for simulating flows with moving particles. *Int. J. Multiphase Flow* **2008**, *34*, 283–302. [CrossRef]
18. Allampalli, V.; Hixon, R.; Nallasamy, M.; Sawyer, S.D. High-accuracy large-step explicit Runge–Kutta (HALE-RK) schemes for computational aeroacoustics. *J. Comput. Phys.* **2009**, *228*, 3837–3850. [CrossRef]
19. Albuquerque, L.A.V.d.; Villela, M.F.d.S.; Mariano, F.P. Numerical Simulation of Flows Using the Fourier Pseudospectral Method and the Immersed Boundary Method. *Axioms* **2024**, *13*, 228. [CrossRef]
20. Canuto, C.; Hussaini, M.Y.; Quarteroni, A.; Zang, T.A. *Spectral Methods: Fundamentals in Single Domains*; Springer: New York, NY, USA, 2006.
21. Lee, M.; Moser, R.D. Direct numerical simulation of turbulent channel flow up to $Re_\tau = 5200$. *J. Fluid Mech.* **2015**, *774*, 395–415. [CrossRef]
22. del Álamo, J.C.; Jiménez, J. Spectra of the very large anisotropic scales in turbulent channels. *Phys. Fluids* **2003**, *15*, L41–L44. [CrossRef]
23. Schlichting, H.; Kestin, J. *Boundary-Layer Theory*, 8th ed.; Springer: Berlin/Heidelberg, Germany, 2017.

Disclaimer/Publisher's Note: The statements, opinions and data contained in all publications are solely those of the individual author(s) and contributor(s) and not of MDPI and/or the editor(s). MDPI and/or the editor(s) disclaim responsibility for any injury to people or property resulting from any ideas, methods, instructions or products referred to in the content.